JGR Solid Earth

RESEARCH ARTICLE
10.1029/2019JB018810

Key Points:
- We inverted *P* waveforms recorded by our BBOBSs to obtain the depth profile of the *P* velocity beneath the older Pacific plate
- Combining our *P* model with a previous *S* model revealed two notable features in V_P/V_S structures
- The obtained V_P/V_S model suggests chemical stratification in the lithosphere and the effects of anelasticity or melt at the LAB

Supporting Information:
- Supporting Information S1

Correspondence to:
N. Takeuchi,
takeuchi@eri.u-tokyo.ac.jp

Citation:
Takeuchi, N., Kawakatsu, H., Shiobara, H., Isse, T., Sugioka, H., Ito, A., & Utada, H. (2020). Inversion of longer-period OBS waveforms for *P* structures in the oceanic lithosphere and asthenosphere. *Journal of Geophysical Research: Solid Earth*, *125*, e2019JB018810. https://doi.org/10.1029/2019JB018810

Received 30 SEP 2019
Accepted 20 JUN 2020
Accepted article online 23 JUN 2020

Inversion of Longer-Period OBS Waveforms for *P* Structures in the Oceanic Lithosphere and Asthenosphere

Nozomu Takeuchi[1], Hitoshi Kawakatsu[1], Hajime Shiobara[1], Takehi Isse[1], Hiroko Sugioka[2], Aki Ito[3], and Hisashi Utada[1]

[1]Earthquake Research Institute, University of Tokyo, Tokyo, Japan, [2]Graduate School of Science, Kobe University, Kobe, Japan, [3]Research Institute for Marine Geodynamics, Japan Agency for Marine-Earth Science and Technology, Yokosuka, Japan

Abstract We performed waveform inversion of the *P* waveforms recorded by our BroadBand Ocean Bottom Seismometers (BBOBSs) deployed in the Northwestern Pacific. Consequently, the depth profile of the *P* velocity of the oceanic upper mantle, which has not been well resolved by previous surface wave or receiver function analyses, was revealed. We considered the azimuthal anisotropy in the lithosphere, which significantly improved the variance reduction from 34% to 44%. The resulting *P* model exhibited higher and lower velocities in the lithosphere and asthenosphere, respectively. The velocity contrast was found to be second/third of that observed in the previous *S* models; however the obtained model appeared to have some trade-off with the V_S structures in the vicinity of the source. We compared our *P* model with the previous *S* model obtained using our BBOBSs and obtained the V_P/V_S model. The resulting V_P/V_S model has two notable features. First, the lithosphere is characterized by a rapid increase in the V_P/V_S values with depth, which implies chemical stratification. Second, the V_P/V_S values in the vicinity of the lithosphere-asthenosphere boundary (LAB) are larger than the synthetic values of any major upper mantle mineral predicted by considering the anharmonic effects, which suggests the effects of anelasticity or melt.

1. Introduction

The oceanic lithosphere and asthenosphere system is one of the most fundamental features of plate tectonics. The oceanic asthenosphere is characterized by a lower *S* velocity and stronger attenuation (lower *Q*), which exhibits sharp contrast with the oceanic lithosphere (e.g., Kawakatsu & Utada, 2017). The origin of the sharp contrast is debated in seismology, geodynamics, and laboratory experiments. It has been previously attributed to either partial melt (Anderson & Sammis, 1970), elevated water content (Hirth & Kohlstedt, 1996), or reduced grain size (Jackson & Faul, 2010). Grain boundary softening by a solid-state mechanism (Takei, 2017; Takei et al., 2014; Yamauchi & Takei, 2016) and flaws in the regular atomic packing under oxidizing conditions (Cline et al., 2018) have also been reported by recent laboratory experiments.

To identify the aforementioned origin, it is essential to provide new constraints on the seismic structures. However, most of the information on the oceanic upper mantle obtained thus far is on the *S* structure. The higher resolution upper mantle models obtained using surface waves (e.g., Debayle et al., 2016; Isse et al., 2019; Schaeffer & Lebedev, 2013) are the *S* models. Global *S* tomography models obtained using broadband waveforms (e.g., Auer et al., 2014; Chang et al., 2015; French & Romanowicz, 2014; Koelemeijer et al., 2016; Kustowski et al., 2008; Moulik & Ekström, 2014; Takeuchi, 2012) have better resolution, whereas many of the *P* tomography models obtained using the *P* traveltime data have poor resolution (e.g., Bijwaard et al., 1998; Boschi & Dziewonski, 1999; Li et al., 2008; Obayashi et al., 2013; Simmons et al., 2012) in the oceanic upper mantle. Some joint inversion models (e.g., Bozdag et al., 2016; Houser et al., 2008) apparently have a better *P* resolution, but it is primarily constrained by the scaling relations between the *P* and *S* anomalies that are assumed a priori. The use of *PP*−*P* traveltimes improves the resolution (e.g., Fukao et al., 2003; Montelli et al., 2004, 2006); however, the improvements are not enough to enable the discussion of the vertical contrast of the oceanic lithosphere and asthenosphere. The depth and contrast of the lithosphere-asthenosphere

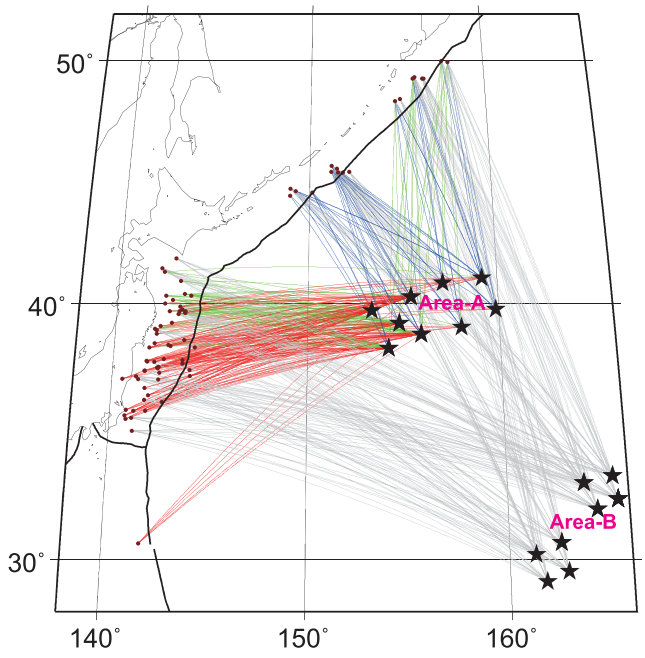

Figure 1. Distribution of events (denoted by deep red circles), stations (black stars), and great circle paths (thin solid lines) used in our analysis. For the data from the stations in Area-A, the azimuth is denoted by the same color used in Figure 5c. Plate boundaries (denoted by thick black lines) are overplotted for reference.

boundary (LAB) are detected using receiver functions (e.g., Kawakatsu et al., 2009; Rychert & Shearer, 2009) or *SS* precursors (e.g., Tharimena et al., 2017); however, they only reveal the *S* structures.

In this study, we focused on the depth distribution of the *P* velocity in the oceanic upper mantle. Between 2010 and 2015, we deployed broadband ocean bottom seismometers (BBOBSs) in the Northwestern Pacific (Figure 1) as a part of the Normal Mantle Project (NOMan Project; http://www.eri.u-tokyo.ac.jp/yesman/). CMG-3T with an eigenperiod of 360 s were the sensors utilized. Because the stations (the black stars in Figure 1) are located at approximately 5–21° from the events in the nearby subduction zones, the *P* waves directly sample the oceanic upper mantle, which provides unique opportunities to reveal the vertical profile of the *P* velocity. The operation periods of the NOMan BBOBSs were more than 4 years, and we conducted repeated observations by recovering old BBOBSs and installing new ones at similar locations every year. These operations obtained an unprecedented quantity and quality of data to reveal the *P* structures of the oceanic lithosphere and asthenosphere.

However, there are several difficulties in analyzing the *P* waves sampling the oceanic upper mantle. First, the waveforms for higher frequencies are complicated owing to strong scattering in the oceanic lithosphere (e.g., Kennett & Furumura, 2013; Kennett et al., 2014; Shito et al., 2013, 2015; Takeuchi et al., 2017). Second, the observed higher-frequency energy sampling the asthenosphere and sub-asthenospheric upper mantle (hereafter referred to as mesosphere) is expected to be significantly small owing to the strong attenuation in the asthenosphere; Q for the *P* wave, Q_P, is estimated to be approximately 100–200 (e.g., Booth et al., 2014; Dalton et al., 2008; Dziewonski & Anderson, 1981; Takeuchi et al., 2017). Finally, it is relatively difficult to resolve the structures within the oceanic asthenosphere because the low velocity zone (LVZ) causes diffracted waves that cannot be described using the conventional ray theory. Therefore, in this study, we inverted the longer-period *P* waveforms (0.01–0.1 Hz) using the full-wave computational method (Direct Solution Method Kawai et al., 2006; Takeuchi et al., 1996). The use of longer-period components minimizes the effect of scattering, and the use of full synthetic waveforms enables us to reveal the LVZ structures by accurately considering the diffracted waves traversing the oceanic asthenosphere. The results obtained by this study can enable us to discuss the V_P/V_S structures in the oceanic upper mantle, which imposes further constraints on the origin of the enigmatic lithosphere-asthenosphere system.

2. Data

We used the vertical component of the BBOBSs deployed under the NOMan project. We deconvolved the instrumental response to obtain the velocity seismogram and applied a bandpass filter with corner frequencies of 0.01 and 0.1 Hz. We individually inspected the *P* waveforms for all shallower events (the centroid depth was shallower than 60 km) with a smaller size (the moment magnitude was smaller than 6.7) in the Global CMT catalog (Ekstrom et al., 2012) that occurred in the Northwestern Pacific region. We selected waveforms with higher quality and used them as the data set for our waveform inversion. We only used the shallower events to ensure that the coherency between the events can be discussed in a straightforward manner. We only utilized the smaller events because their source-time functions are expected to be simple. The resulting data set comprised 541 traces for 76 events (Figure 1).

To discuss the features of the observed data, we defined an appropriate reference model. We employed the IASP91 model (Kennett & Engdahl, 1991) as the reference model because, generally, this model efficiently explains the *P* traveltimes, one of the primary types of information contained in our data set. However, because our primary target is the oceanic region, there are several inconvenient limitations in the IASP91 model, which is designed to explain continental data. First, the model does not include the sea water layer. Second, the model assumes that the sensor is on the surface, whereas the actual OBS is located on the ocean

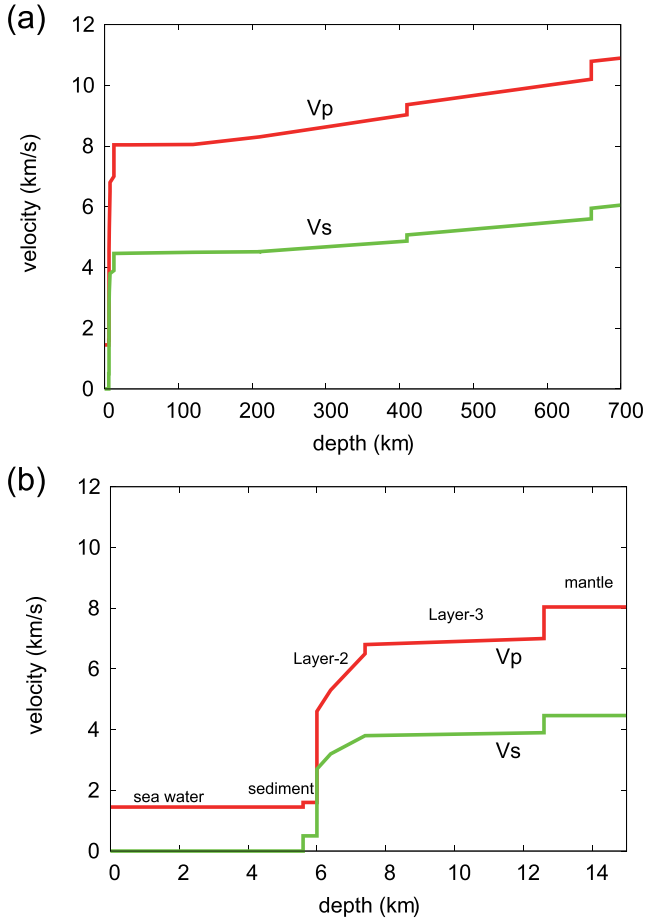

Figure 2. (a) Assumed reference model used to discuss the features of the observed data. (b) Enlarged picture of the crustal part of the model shown in (a).

bottom. Finally, the crustal part of IASP91 is a continental model instead of an oceanic model. Therefore, we replaced the crustal part of the IASP91 model with the oceanic crust model obtained by a survey conducted in the easternmost region of our array in Area-A (see Figure 1) (Shinohara et al., 2008) and utilized it as the reference model (Figure 2). Because we also required the density and Q structures to compute the synthetic seismograms, we assumed the values in PREM (Dziewonski & Anderson, 1981), with the locations of the internal discontinuities being appropriately shifted to match those in the reference model.

Figure 3a shows a record section of the observed waveforms inverted in this study. A blow-up figure for closer distances is also shown (Figure 4a). A zero phase bandpass filter of 0.01–0.1 Hz is applied. The time is with respect to the synthetic initial P arrival time computed for the reference model. The source depths are corrected to the seafloor surface, and the distances are accordingly corrected.

To visualize the arrival timing of the initial P packet, we measured the traveltime residuals by cross-correlating an observed waveform with a synthetic waveform computed for the reference model (Figure 5a). To isolate the first packet more efficiently, in these traveltime measurements, we applied a causal bandpass filter of 0.01–0.1 Hz and used seismograms between −15 s and 10 s to the synthetic initial P arrival time. While computing the synthetic seismograms, we assumed the centroid location, centroid moment tensors, and half duration time in the Global CMT catalog (Ekstrom et al., 2012). The results demonstrated (i) earlier arrivals at smaller distances (of approximately 6–8°), (ii) a rapid increase in the residuals (i.e., a significantly slow apparent velocity) at distances in the neighborhood of 12°, and (iii) an increase in the residual at larger distances (beyond approximately 16°). These features were also confirmed in the record section shown in Figures 3a and 4a.

Although our primary focus in this study is to reveal the isotropic part of the structure in the oceanic upper mantle, the observed traveltime residuals may be affected by the anisotropy in the lithosphere. The lithospheric anisotropy is suggested to exist in the Northwestern Pacific (e.g., Nishimura & Forsyth, 1989; Shimamura et al., 1983; Shinohara et al., 2008; Takeo et al., 2018), while the azimuthal anisotropy in the asthenosphere is suggested to be weak (Takeo et al., 2018). If we categorize the data according to the azimuth of the raypath, the data propagating in faster directions show systematically earlier arrivals (Figure 5b). The categories are defined in terms of the model of Shinohara et al. (2008); if the P velocity for the azimuth of the raypath is in upper, middle, and lower one-thirds of the P velocity range of the model, we categorize the data in the faster, moderate, and slower directions, respectively. Note that the direction of the azimuthal anisotropy of Shinohara et al. (2008) is generally consistent with that of the model for Area-A (Figure 1) by Takeo et al. (2018), who performed two-station analysis of surface waves observed by our arrays. The results in Figure 5b indicate that the observed residuals at smaller distances (up to approximately 12°) can be biased by the lithospheric anisotropy and show the importance of considering the anisotropy in waveform inversion.

3. Method

In the waveform inversion performed in this study, we first inferred the anisotropic structure in the lithosphere and then inverted the waveforms for the isotropic part of the structures of the oceanic upper mantle. We also performed the inversion without considering the lithospheric anisotropy and compared the resultant models. Accordingly, we checked the magnitude of the trade-off between the lithospheric anisotropy and the isotropic part of the upper mantle structure.

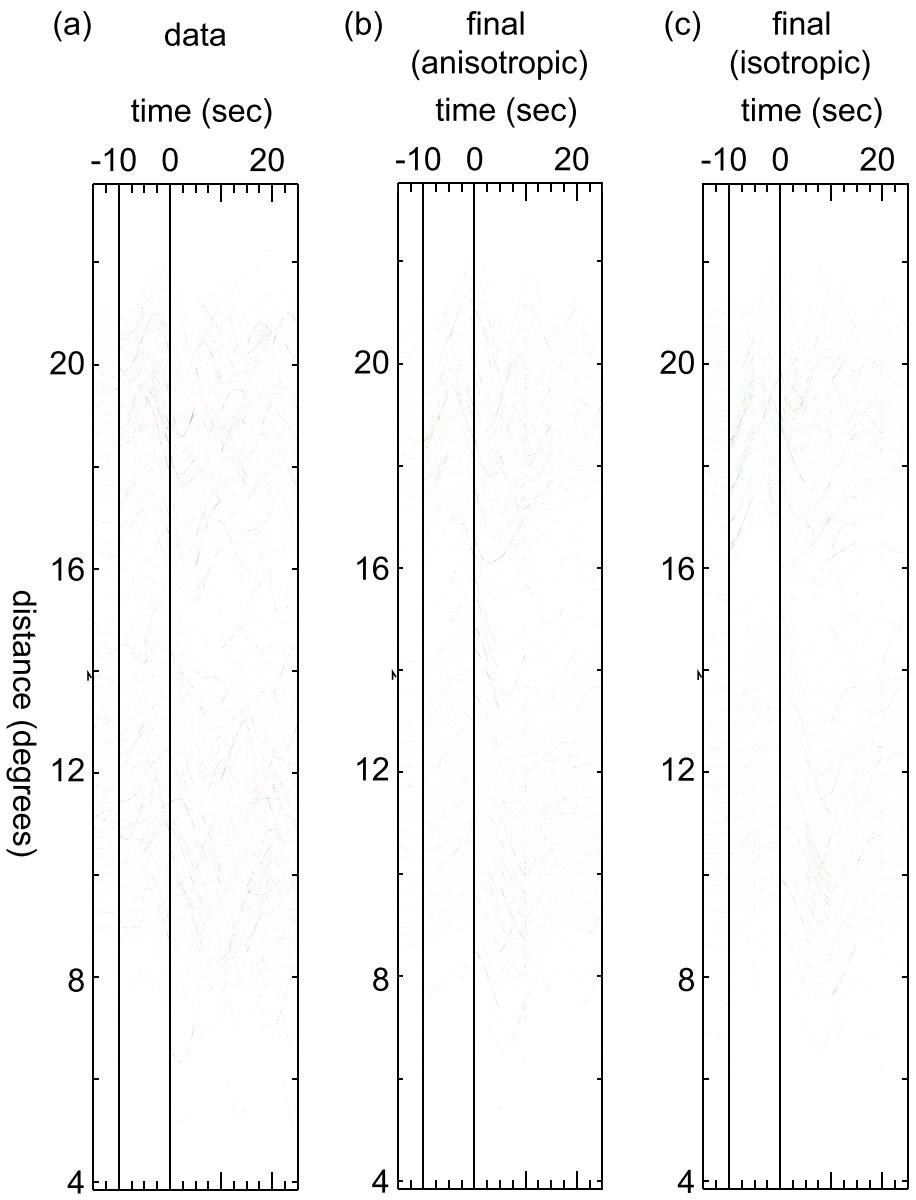

Figure 3. (a) Observed waveforms analyzed in this study. A zero phase bandpass filter with corner frequencies of 0.01 and 0.1 Hz is applied. The horizontal axis denotes the time with respect to the synthetic initial *P* arrival time computed for the reference model (Figure 2). Vertical lines are overplotted at −10 s and 0 s for reference to observe the onset timing and broadening of the first packets. The vertical axis denotes the distance from the hypocenter with source depth correction to the seafloor surface. (b) Same as (a), except that the synthetic waveforms for the final anisotropic model are shown. (c) Same as (b), except that the synthetic waveforms for the final isotropic model are shown.

3.1. Model Parameters for Anisotropy in the Lithosphere

We defined a region $6{,}283.4 \leq r \leq 6{,}358.4$, where r denotes the radius in kilometers, as the lithospheric part. Note that $r = 6{,}283.4$ (87.6 km depth) represents the location of the LAB detected by Kawakatsu et al. (2009), and $r = 6{,}358.4$ (12.6 km depth) represents the Moho location of the reference model. We introduced anisotropy in this region. We considered a weak azimuthal anisotropy embedded in the isotropic structure whose density and *P* and *S* velocities are given by $\rho(r)$, $V_P(r)$, and $V_S(r)$, respectively. We assumed that the azimuthal dependence of the horizontal *P* velocity can be written in the general form for weak anisotropy (Backus, 1965):

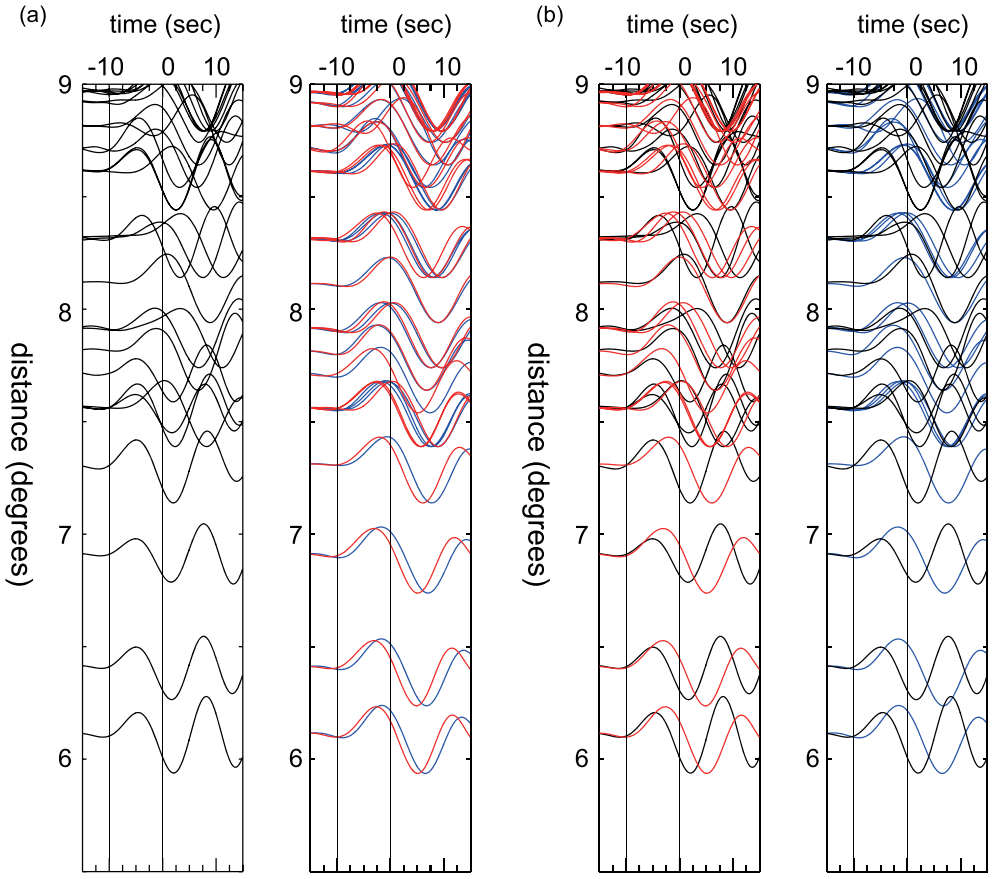

Figure 4. Enlarged representation of Figure 3. (a) Observed waveforms (black) and synthetic waveforms for the final anisotropic model (red) and final isotropic model (blue). (b) Same as (a), except that the observed and synthetic waveforms are directly compared.

$$\frac{\alpha_h(r,\varphi)-V_P(r)}{V_P(r)}=\epsilon^{(2)}\cos 2\left(\varphi-\varphi_m^{(2)}\right)+\epsilon^{(4)}\cos 4\left(\varphi-\varphi_m^{(4)}\right), \tag{1}$$

where α_h is the horizontal P velocity (i.e., velocity of the horizontally traveling P wave), φ is the azimuth, $\varphi_m^{(i)}$ is the azimuth of the maximum velocity, and $\epsilon^{(i)}$ denotes the coefficients that describe the strength of the azimuthal dependence. Note that we assumed that $\epsilon^{(i)}$ and $\varphi_m^{(i)}$ are depth independent, and $\epsilon^{(i)}\ll 1$. In the discussions below, we only consider the first-order terms of $\epsilon^{(i)}$ and ignore the higher-order terms.

To simplify the problem, we appropriately extrapolated the P and S velocities from the anisotropy parameters, $\epsilon^{(i)}$ and $\varphi_m^{(i)}$, in Equation 1. Because our data set is primarily sensitive to horizontal P velocities, these assumptions will not change the primary features of the models obtained below. We used the following assumptions: (i) the vertical P velocity (i.e., velocity of the vertically traveling P wave), $\alpha_v(r,\varphi)$, is independent of the azimuth φ and is equal to the isotropic part of the velocity $V_P(r)$, (ii) the P velocity of the azimuth φ and incident angle θ, $\alpha(r,\varphi,\theta)$, is given by $\left[\alpha_v(r,\varphi)\cos^2\theta+\alpha_h(r,\varphi)\sin^2\theta\right]$, and (iii) the S velocities are completely isotropic (i.e., independent of the azimuth φ, incident angle θ, and polarization) and are equal to the isotropic part of the velocity, $V_S(r)$. These assumptions imply that for each azimuth of φ, the velocity surface (the dependence of the incident angle θ) is that for the radial anisotropy satisfying the "elliptic condition" (Thomsen, 1986). We can also state that for each azimuth, the velocity surface is that for the radial anisotropy with $\eta_\kappa=1$, where η_κ is the new fifth parameter for the transverse isotropy defined by Kawakatsu (2016). We illustrated the extrapolated velocity surfaces in supporting information Figure S1 with additional explanations (Text S1). As evident in Figure S1, the effects of anisotropy become weaker for smaller incident angles (i.e., larger distances), which is consistent with the observations (Figure 5b).

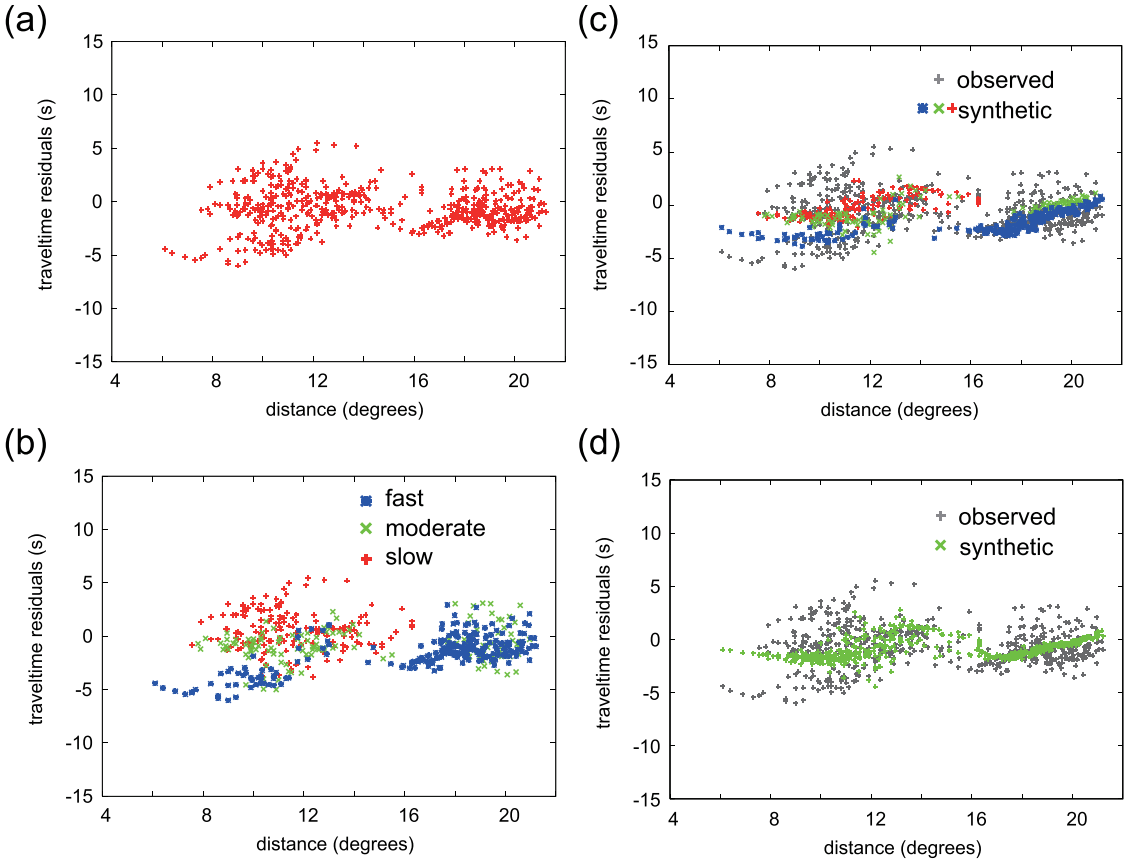

Figure 5. (a) Traveltime residuals measured by cross-correlating the observed waveform and synthetic waveform computed for the reference model. (b) Same as (a), except that the data points are classified in terms of the azimuth of the raypath. See the text for details. (c) Comparison of the traveltime residuals measured for the observed waveforms (gray) and the synthetic waveforms computed for the final anisotropic model (blue, green, and red). (d) Comparison of the traveltime residuals measured for the observed waveforms (gray) and the synthetic waveforms computed for the final isotropic model (green). In all figures, source depth corrections to the seafloor surface were applied.

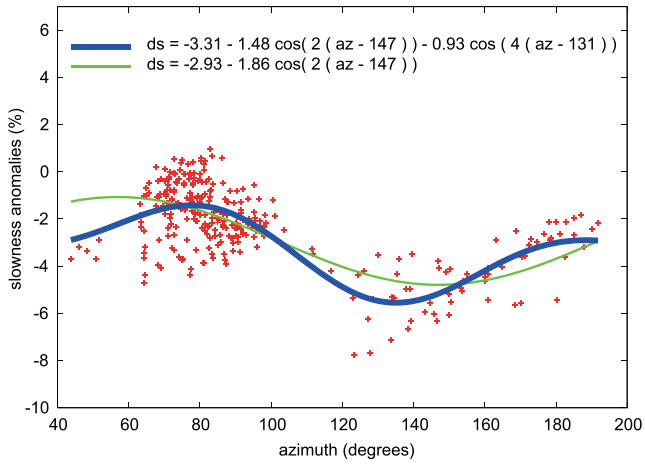

Figure 6. Azimuthal distribution of the observed slowness anomalies of higher-frequency *Pn* waves (red crosses). Regression curves for the case with and without *4Ø* terms are plotted with thick blue and thin green lines, respectively.

3.2. Inference of Anisotropic Parameters

We inferred the anisotropic parameters, $\epsilon^{(i)}$ and $\varphi_m^{(i)}$, in Equation 1 using the traveltimes measured from the higher-frequency *Pn* waveforms. From the waveform traces in our data set, we selected those with an initial phase of *Pn* (i.e., the *P* wave bottoming inside the lithosphere) for the reference model. We then applied a causal high pass filter with corner frequencies of 2 Hz and handpicked the onset of the *Pn* waves. The picked onset times were translated to the averaged slowness anomalies on the raypath within the lithosphere. We plotted each slowness anomaly as a function of the azimuth and inferred the anisotropic parameters (Figure 6).

The largest and smallest slowness anomalies were observed at approximately 80° and 140° of the azimuth, respectively. This indicates that the fastest and slowest azimuths are not orthogonal, and the cos4φ term in Equation 1 is critical. When we fit the observations without the cos4φ term (i.e., with the assumption $\epsilon^{(4)} = 0$), the regression curve (the green line in Figure 6) cannot explain the observations well. The importance of the cos 4φ term has also been suggested by a previous study in the old Pacific plate (Shintaku et al., 2014). From the regression curve with the cos4φ term (the blue line in Figure 6), we inferred the anisotropic parameters as follows:

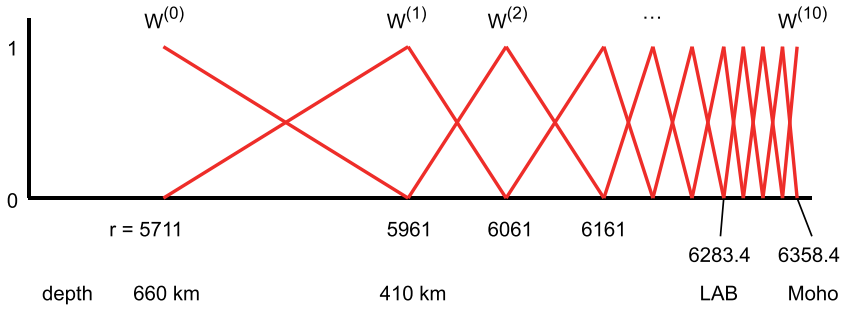

Figure 7. Linear spline functions, $W^{(m)}(r)$, used to define model parameters for the isotropic part of the *P* velocity structure.

$\epsilon^{(2)} = 1.48$, $\epsilon^{(4)} = 0.93$, $\varphi^{(2)} = 147°$, and $\varphi^{(4)} = 131°$. Note the difference in sign between the slowness and velocity anomalies. Our result (the blue line) shows the peak-to-peak amplitude and the direction of the fastest azimuth, similar to those obtained by Shinohara et al. (2008); however, the direction of the slowest azimuth is somewhat different. Our result shows a significantly smaller peak-to-peak amplitude than that obtained by Shimamura et al. (1983), and the directions of the fastest and slowest azimuth are somewhat different.

Owing to the limited event-station coverage, the data set for each azimuthal range basically comprised specific event-array pairs. All waveform traces with an initial phase of *Pn* were recorded by the northwestern array in Figure 1, and, in general, the data for a larger event latitude were found to have a larger azimuth (see Figure 1). This implies that the sampling regions for each azimuthal range are different, and the above parameters may be biased by the lateral heterogeneities in the lithosphere. Therefore, we should assume that the aforementioned parameters correct both the anisotropy and heterogeneity of horizontal *P* velocities in the lithosphere. Because we aim to perform the corrections required to infer the isotropic part of the radial dependent structure, such parameters are preferable for the analysis of *Pn* and other horizontal *P* waves, even though we cannot correct the effects of heterogeneities of the vertical *P* velocities.

3.3. Model Parameters for the Isotropic Part

We expanded the perturbation of the isotropic part of the *P* velocity from the *P* velocity of the initial reference model, $V_P^{(0)}(r)$, in terms of the linear spline functions $W^{(m)}(r)$,

$$\frac{V_P(r) - V_P^{(0)}(r)}{V_P^{(0)}(r)} = \sum_m \delta c_m W^{(m)}(r), \tag{2}$$

and defined δc_m as the model parameter. In this study, the node locations of the linear spline functions $W^{(m)}$ $(0 \le m \le 10)$ were defined as shown in Figure 7. Note that we only perturbed the *P* structure in the upper mantle (5,711.0 $\le r \le$ 6,358.4). There are discontinuities in the initial reference model at r = 5,711.0, 5,961.0, and 6,358.4 km (depths of 660, 410, and 12.6 km depth, respectively), and we set the nodes there. We also set a node at r = 6,283.4 km (87.6 km depth), where the LAB was assumed.

Because our data set is primarily sensitive to the *P* structures, the resolving power for *S* structures is limited. We therefore assumed the following scaling relation:

$$\frac{V_S(r) - V_S^{(0)}(r)}{V_S^{(0)}(r)} = 2\left(\frac{V_P(r) - V_P^{(0)}(r)}{V_P^{(0)}(r)}\right), \tag{3}$$

where $V_S^{(0)}(r)$ is the *S* velocity of the initial reference model. This is one of the scaling relations assumed in previous studies (e.g., French & Romanowicz, 2014; Panning & Romanowicz, 2004). Other previous studies used a smaller (e.g., Houser et al., 2008) or larger (e.g., Ritsema et al., 2011) scaling factor than 2 in Equation 3.

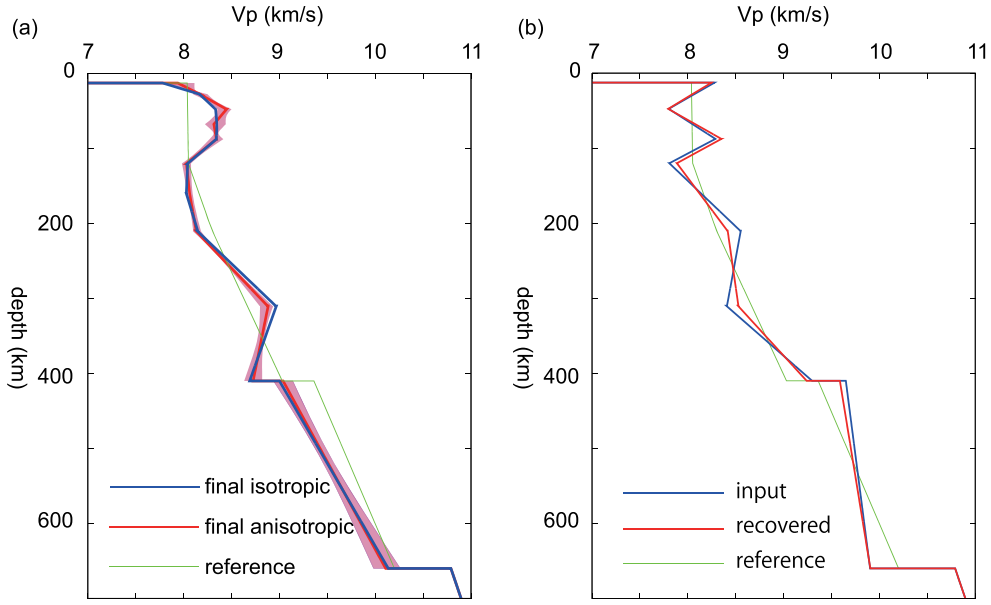

Figure 8. (a) Comparison of the obtained models and the reference model. The final anisotropic model (red), final isotropic model (blue), and reference model (green) are shown. The shaded regions denote the estimated 2σ errors of the final anisotropic model. (b) Results of the recovery test. The input and recovered models are shown in blue and red, respectively. The reference model, that is, the initial model of this test, is shown in green.

3.4. Explicit Procedures for Waveform Inversion

We assumed the anisotropic parameters, $\epsilon^{(i)}$ and $\varphi_m^{(i)}$ in Equation 1, obtained in section 3.2 and inverted the P waveforms for the isotropic part of the model, δc_m in Equation 2. We first assumed that the lithospheric anisotropy is embedded in the reference model (Figure 2) and defined it as the initial model of the inversion for the isotropic part of the structure. We fixed the source parameters to the global CMT solutions (Ekstrom et al., 2012) with the triangular source-time function. Our data set comprised the P wave part of the waveforms with a duration of 40 s (between −15 and 25 s to the synthetic initial arrival time for the initial reference model; Figure 3a). To extract the phase information with equal weights from each trace, we normalized the r.m.s. amplitude of the trace.

We linearized the inverse problems and iteratively searched solutions until convergence was achieved (four iterations). In each iteration, we computed the synthetic seismograms and their partial derivatives for the structure, including the azimuthal anisotropy in the lithosphere. However, huge computational resources are required for rigorously computing synthetics for models with azimuthal anisotropy. In this study, we therefore adopted the approximated method. For each event and station pair, we defined an "equivalent radial anisotropic structure" with the same P and S velocity surfaces for the given azimuth φ (see Figure S1). The explicit form of the elastic moduli equivalent to the azimuthal anisotropy defined in section 3.1 is given as follows:

$$\begin{aligned}
A(r,\varphi) &= \rho(r)V_P(r)^2\left[1+2\epsilon^{(2)}\cos 2\left(\varphi-\varphi_m^{(2)}\right)+2\epsilon^{(4)}\cos 4\left(\varphi-\varphi_m^{(4)}\right)\right]\\
C(r,\varphi) &= \rho(r)V_P(r)^2\\
N(r,\varphi) &= \rho(r)V_S(r)^2\\
L(r,\varphi) &= \rho(r)V_S(r)^2\\
F(r,\varphi) &= \rho(r)V_P(r)^2\left[1+\epsilon^{(2)}\cos 2\left(\varphi-\varphi_m^{(2)}\right)+\epsilon^{(4)}\cos 4\left(\varphi-\varphi_m^{(4)}\right)\right]-2\rho(r)V_S(r)^2.
\end{aligned} \tag{4}$$

This is one of the great circle approximations that was widely used in previous global tomographies (e.g., Megnin & Romanowicz, 2000; Woodhouse & Dziewonski, 1984). Even if we use this approximation, a long CPU time is required because the synthetic seismograms and their partial derivatives must be computed for

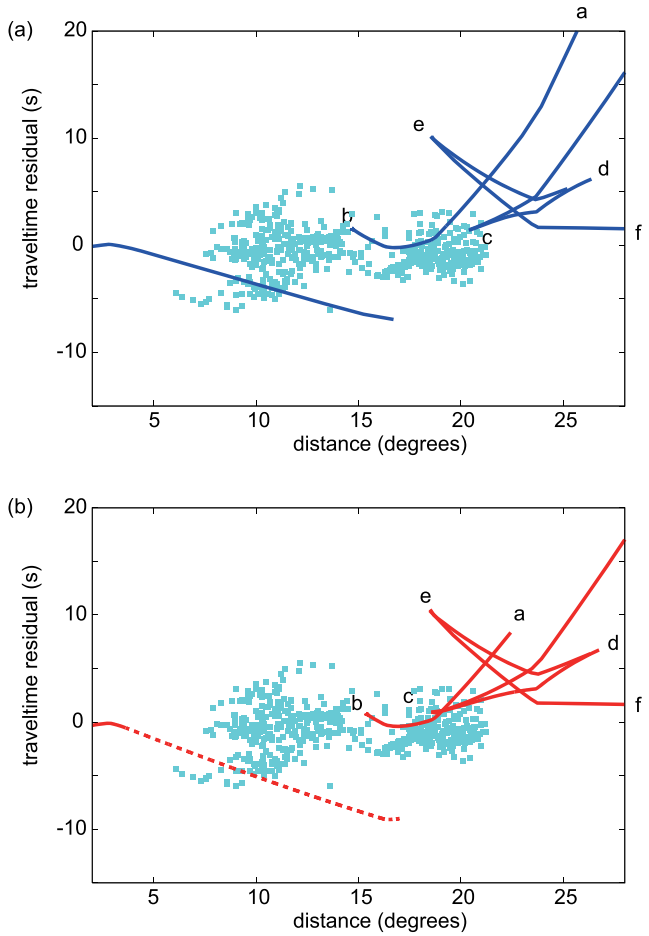

Figure 9. (a) Traveltime curves (solid lines) for the final isotropic model in Figure 8a (dark blue). Observed traveltime residuals are also plotted in light blue. Source depth corrections to the seafloor surface were applied. (b) Same as (a), except that the traveltime curves for the final anisotropic model are plotted. The dotted line denotes the diffracted *Pn*. The labels from a to f in the traveltime curves denote the corresponding cusp locations for the isotropic (a) and anisotropic (b) cases.

various equivalent models; the number of models is the same as the number of waveform traces in the data set (541 different models for this study). However, each iteration of the inversion can be completed in approximately 36 hr if the cluster system of our institute with 432 cores is utilized.

4. Results

4.1. Obtained Model

The obtained isotropic part of the *P* structure, $V_P(r)$, is depicted by the red line in Figure 8a. Hereafter, the obtained model is referred to as the "final anisotropic model." We estimated the errors of the obtained model by the bootstrap method using 10 bootstrap samplings of our data set; the 2σ errors are represented by the shaded region in Figure 8a. The explicit V_P values and their estimated errors are presented in Table S1. For comparison, we also tested the case without anisotropy in the lithosphere (i.e., we assumed $\epsilon^{(i)} = 0$), and the obtained model is referred to as the "final isotropic model" (the blue line in Figure 8a). The variance reductions for the final anisotropic and isotropic models were 44% and 34%, respectively, and the incorporation of lithospheric anisotropy improved the variance reduction. However, the final anisotropic and isotropic models exhibited similar features for the isotropic part of the model (Figure 8a). The velocity contrast between the lithosphere and asthenosphere (the maximum and minimum velocities in the lithosphere and the asthenosphere, respectively) was found to be 5.1% and 3.9% for the final anisotropic and isotropic models, respectively.

The comparisons between the synthetic seismogram for the obtained models and the observed seismogram are shown in Figures 3 and 4. The onset time of the synthetic waveforms at closer distances demonstrated systematic differences between the final anisotropic and isotropic models, and the final anisotropic model better explained the observations (Figure 4b). The traveltime residuals were also measured for the synthetic seismograms for the final anisotropic and isotropic models; additionally, they were compared with those measured for the observed seismograms in Figures 5c and 5d. The final isotropic model can explain the rapid increase in the residuals at distances in the neighborhood of 12° to some extent (Figure 5d); however, by introducing the lithospheric anisotropy, we can explain the systematic earlier arrivals in faster directions and better fit the traveltime residuals (Figure 5c).

On comparing the final anisotropic model and the reference model (the red and green lines in Figure 8a), it is evident that the primary features of the final anisotropic model include (i) anisotropy in the lithosphere, (ii) higher and lower velocity anomalies in the oceanic lithosphere and asthenosphere, respectively, and (iii) lower velocity anomalies in the vicinity of the 410 discontinuity. To confirm whether we have sufficient resolution, we show the result of our resolution test in Figure 8b. We inverted the synthetic data computed for the input model (the blue line in Figure 8b) using the same procedure that was used to obtain the models in Figure 8a. Because the variance reduction is approximately 50% for the final anisotropic model, we added 50% random noise to the synthetic data. The recovered model reproduced the input model approximately up to 210 km depth (Figure 8b). Therefore we only discuss lithospheric and asthenospheric structures below. The final anisotropic model in Figure 8a presents somewhat corrugated structures in the lithosphere, which may be due to the parameterization with the linear spline functions (Figure 7). To confirm that such corrugations do not affect the discussions below, we performed inversion using different regularizations, which are present in Figure 10a. We confirmed that the model changed slightly in the lithosphere and asthenosphere.

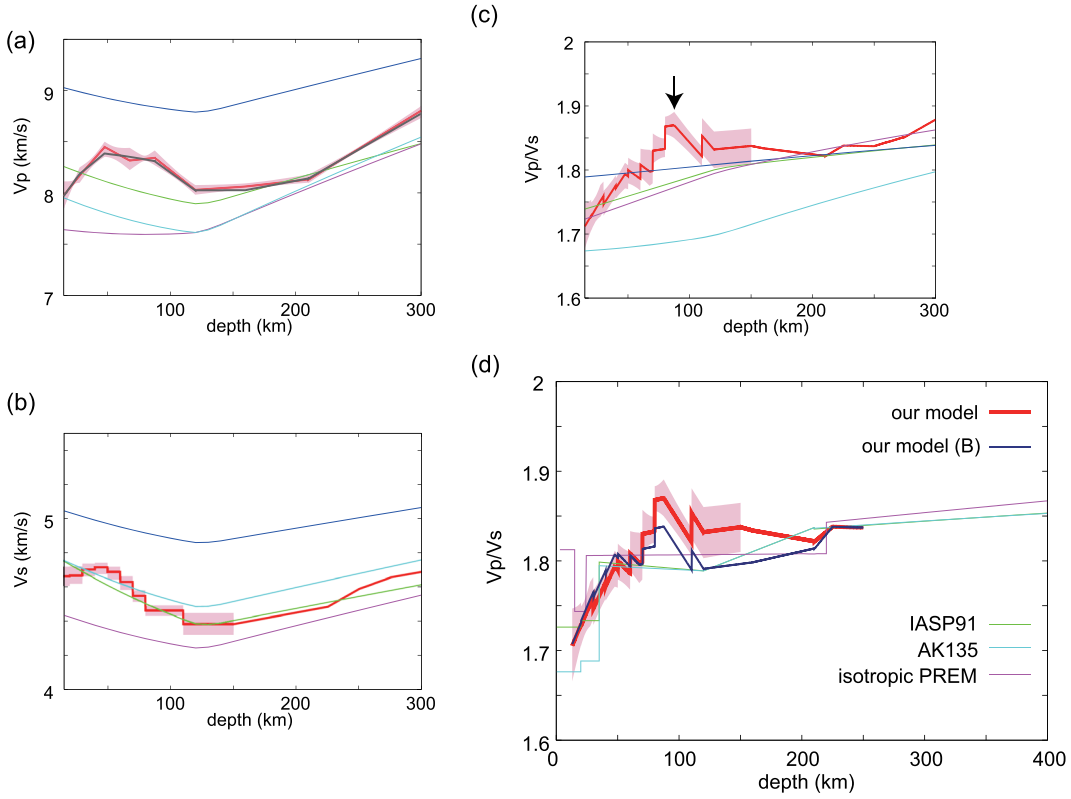

Figure 10. (a) Comparison between our P model (red) and synthetic V_P values of major upper mantle minerals (olivine in green, garnet in blue, clinopyroxene in purple, and orthopyroxene in light blue). The P model obtained using the smoothness constraints (gray) is also plotted. See the text for details. (b) Comparison of the S model of Takeo et al. (2018) (red) and synthetic V_S values of major upper mantle minerals denoted by the same color conventions as in (a). (c) Comparison between our V_P/V_S model (red) and synthetic V_P/V_S values of major upper mantle minerals denoted by the same color conventions as in (a). The black arrow denotes the location of the LAB. (d) Comparison between our V_P/V_S model (red) and representative standard Earth models: IASP91 (Kennett & Engdahl, 1991) (green), AK135 (Kennett et al., 1995) (light blue), and isotropic PREM (Dziewonski & Anderson, 1981) (purple). For reference, our V_P/V_S model obtained using the V_S model in Area-B is also plotted (blue). In all figures, the shaded regions denote the estimated 2σ errors.

4.2. Regional Variations of the Observed Waveforms

The obtained model could explain the overall features of the observed waveforms (Figures 3 and 5c); however, we found that both the observed waveforms and degree of waveform fitting are regionally dependent. To confirm this, we defined two data bins such that the data in each data bin sample similar regions with similar azimuths (Text S2 and Figure S2) and separately compared the observed and synthetic waveforms (Figures S3–S5).

For Data Bin 1, the observed waveforms, including the later packets, could be explained relatively accurately (Figure S3); however, some waveforms demonstrated a systematic delay in the first packet (Figure S4). The raypaths of the delayed data are depicted by the red lines in Figure S1. Such anomalies are more pronounced if the magnified record sections are shown at closer distances (Figure S6); for example, it was observed that the waveforms abruptly change at approximately 7.9° and 8.2°. The anomalous waveforms in Figure S4 show either a more emergent onset (at approximately 7.9°, for example) or a narrower packet (at approximately 9.0°, for example) than the synthetic seismograms. As will be discussed later, the initial packet is basically an overlapping phase composed of the initial (*Pn* or *Pn*dif) and secondary direct phases. These results suggest that the anomalies occur when the amplitude of the initial phase is significantly smaller than that of the synthetic seismograms.

For Data Bin 2, the waveform fits were observed to be poor for the later phases (such as the secondary direct phase and depth phases) at smaller distances (Figures S5 and S7). This is because strong reverberations exist

after the initial phase, up to approximately 10°. The reason for these reverberations has not been resolved, but the back-scattered waves confined to the lithosphere (Kennett & Furumura, 2013) may be one of the possibilities. Even at smaller distances, we could obtain a fit for the initial portion of the initial packet (i.e., the initial phase) using the final anisotropic model (Figure S5).

These features have been appropriately confirmed in the record section for specific events (Figure S8); only the initial onset of *P* could be fitted for the event contained in Data Bin 2 (Figure S8c), while the initial and later phases could be both fitted for the event contained in Data Bin 1 (Figure S8a). We also confirmed that the onset time can be better explained by the final anisotropic model (Figures S8ac and S8bd).

The above regional variations precisely explain the observed scatter in the traveltime residuals shown in Figure 5c. If we exclude the anomalous waveforms in Data Bin 1, the observed residuals become closer to the synthetic residuals (Figure S9). Note that the measured residuals are for the overlapping phases of the initial phase (*Pn* or *Pn*dif) and later phases, rather than for an isolated phase. If the amplitude of the initial phase is smaller than that of the synthetic seismograms, the measured residuals become larger. We also observed systematic shifts at closer distances (denoted by the blue symbols up to approximately 10° in Figures 5c and S9); however, such shifts can be interpreted to result from the overlapping of strong reverberations in Data Bin 2. As shown in Figure S8c, the strong reverberations shift the energy centroid earlier.

To test the effects of the biases resulting from the aforementioned regional variations, we separately inverted Data Bins 1 and 2 under the assumption of isotropy and compared the obtained models with the final isotropic model (Figure S10a). The results showed that the final isotropic model effectively averages the two models for the uppermost 210 km, which demonstrates that the effects of the lateral heterogeneities are largely canceled out, at least for the lithospheric and asthenospheric structures. Furthermore, the apparent discrepancies in the lithospheric structures between Data Bins 1 and 2 appear to be largely due to the anisotropy. If we correct the lithospheric anisotropy using the parameters obtained in Figure 6, both models approach the final anisotropic model (Figure S10b). We will show later in this paper that the uncertainties presented in Figure S10 are unlikely to affect the conclusions of this study. Evidently, the obtained 1-D model in Figure 8a is an averaged structure and does not represent the true velocity structure of specific regions. In the discussions below, we first identify the features using the averaged 1-D model and confirm that the identified features can be verified using the models for Data Bins 1 and 2 in Figure S10.

4.3. Robustness of the Obtained Model

One of the largest uncertainties in the models obtained by this study include the effects of the V_S structures. In this study, we assumed the scaling relation of Equation 3 instead of performing inversions for the V_S structure. The obtained V_S structure was found to be completely different from the previous V_S models in this region (e.g., the Area-A model of Takeo et al. (2018) obtained by regional surface wave analysis; see Figure S11a). The V_S model in the final anisotropic model had lower and higher velocities in the upper and lower parts of the lithosphere, respectively, than the Area-A model of Takeo et al. (2018).

To verify how the V_S structures affect the synthetic seismograms, we compared the synthetic seismograms computed for two different models (Figure S12); (i) the V_P and V_S models of the final anisotropic model and (ii) the same model but the V_S structure of the final anisotropic model was replaced with that of the Area-A model of Takeo et al. (2018) for the top 210 km (smoothing by polynomial functions was applied; denoted by the blue line in Figure S11a). We can observe that the initial packets are significantly close to each another, but significant differences exist in the later packets. In the synthetic seismograms for the latter model, the later packets arrived earlier; this implies that the V_S structure in the shallower regions should strongly affect the waveforms (see Figure S11a). These results suggest that the V_S structures primarily affect the depth phases and have minimum effect on the direct phases.

To observe the degree of uncertainties in the obtained model resulting from the V_S structures, we performed a test inversion. In this test, we inverted for the V_P structure and fixed the V_S structure to the model denoted by the blue line in Figure S11a. The results demonstrated that (1) the V_P velocities in the uppermost mantle decrease; (2) the V_P velocity gradient in the upper portion of the lithosphere becomes steeper, and (3) the V_P velocities in the lower portion of the lithosphere increase (Figure S11b). Because we assumed higher V_S velocities in the uppermost mantle, these results may be interpreted as follows: (1) To achieve similar arrival

times for the later packets, lower V_P velocities are required in the uppermost mantle (at approximately Moho-30 km depths); and (2) to achieve similar arrival times for the initial packets, higher V_P velocities are required in the deeper regions (at approximately 40–80 km depths) (i.e., steeper velocity gradient in the shallower lithosphere and larger V_P values in the deeper lithosphere). By comparing the degrees of waveform fitting (Figures S8ac and S13ab), it can be observed that the model obtained by this test inversion degrades the fitting of the initial phases. This model improves the fitting of the later phases of Data Bin 2 (compare Figures S8c and S13b), but it slightly degrades the total variance reduction from 44% to 42%. These results show that assuming plausible oceanic V_S structures is not necessarily effective.

In the discussions below, we use the V_P structure of the final anisotropic model as a plausible model in this region. The source side V_S structures should affect the waveforms because they affect the amplitudes and timing of the depth phases. Because the events occur in the subduction zone, the V_S structures in the subduction zone (e.g., lower velocities in the mantle wedge and higher velocities in the subducting slab) should be considered. Although we do not intend to resolve these structures, the V_S model in our final model somewhat mimics such structures in the shallower portion of the lithosphere whose V_S structures are sensitive to the depth phases (Figure S11a). It is an important future research topic to solve this trade-off problem. However, we believe that it is worth noting that, as will be shown in the next section, interesting and important features can be discussed and are beginning to be imaged using the V_P model obtained via in situ BBOBS observations.

5. Discussion

5.1. Velocity Contrast Between Lithosphere and Asthenosphere

In this study, we quantified the *P* structures in the Northwestern Pacific, where the seafloor age is approximately 100–150 Ma (Seton et al., 2012). To identify the primary information source constraining the lower *P* velocities in the asthenosphere, we plotted the synthetic traveltime curves for the final isotropic and anisotropic models (Figure 9). Note that the anisotropic model considered here is the isotropic part of the structures of our preferred model. At closer distances, we can observe *Pn* (the *P* wave bottoming inside the lithosphere) up to approximately 17° and 4° for the final isotropic and anisotropic models, respectively; however, beyond that distance, its diffracted waves can be observed (hereafter referred to as *Pn*dif). The ab, cd, and ef branches are the *P* wave bottoming in the mesosphere, transition zone, and lower mantle, respectively. Before the *b* cusp, the diffracted waves traversing the asthenosphere can be observed (hereafter referred to as *Pb*dif).

We observed a rapid increase in the traveltime residuals at distances in the neighborhood of 12° (Figure 5a). It is notable that the observed residuals between approximately 6° and 15° are mostly located between the arrival timings of *Pn*dif and *Pb*dif (Figure 9), and they are close to *Pn* (or *Pn*dif) and *Pb*dif in the neighborhood of 6° and 15°, respectively. In this distance range, we have two phases, *Pn* (or *Pn*dif) and *Pb*dif; however, they overlap with each other in longer-period waveforms of 0.01–0.1 Hz. The apparent residuals in Figure 5a depend on how the two phases overlap. As the distance increases and approaches the distance of the *b* cusp, the amplitude of *Pn* (or *Pn*dif) decreases relative to *Pb*dif. The apparent residuals are expected to be close to the arrival times of *Pn* (or *Pn*dif) at smaller distances, but they gradually approach those of *Pb*dif. The magnitude of the increase in the apparent residuals in this distance range should therefore be sensitive to the offset between the traveltime branches of *Pn* (and *Pn*dif) and *Pb*dif, which provides important information on the velocity contrast between the lithosphere and asthenosphere. Therefore, the larger delays of approximately 5 s in the observed apparent residuals (Figure 5a) constrain the larger velocity contrasts of 5.1% and 3.9% in the final isotropic and anisotropic models (Figure 8a), respectively.

Several previous studies quantified the *S* structures in this region using surface waves (e.g., Nishimura & Forsyth, 1989; Takeo et al., 2018) and receiver functions (Kawakatsu et al., 2009; Kumar et al., 2011). Nishimura and Forsyth (1989) performed surface wave tomography and inferred an *S* velocity contrast of 7.6% between the lithosphere and asthenosphere in the oldest part of the Pacific (>110 Ma). Takeo et al. (2018) analyzed our NOMan array for *S* structures beneath the northwestern (Area-A) and southeastern (Area-B) subarrays (see Figure 1) and inferred a contrast of 7.3% and 4.2% for Area-A and Area-B, respectively. Kawakatsu et al. (2009) and Kumar et al. (2011) performed a receiver function analysis and detected an *S* velocity jump of 7–8% in the Northwestern Pacific. These results suggest that the *S* velocity has a

contrast of approximately 7% in the Northwestern Pacific. The final anisotropic and isotropic models (Figure 8a) demonstrated a P velocity contrast of 5.1% and 3.9%, respectively, implying that the P velocity drop in the asthenosphere is approximately 2/3 of the S velocity drop.

To determine whether the obtained model can be interpreted by simple temperature and pressure effects, we compared our P model (the final anisotropic model) and the S model of Takeo et al. (2018) with the synthetic V_P and V_S values predicted by pure anharmonic effects (Figures 10a and 10b). We believe that these are currently the best available models for minimizing the biases caused by limited resolutions. In Figure 10a, we also plotted the V_P model obtained using different regularizations (smoothness constraints instead of norm damping) and verified that the model is significantly consistent with the final anisotropic model. The results showed that our models have good resolution and they are mostly constrained by the observed data, instead of the a priori information assumed in the inversion. The V_S model by Takeo et al. (2018) has better resolution than other S models in this region because they constrained the regional V_S structures using in situ BBOBS observations. The errors for the V_P and V_S models were estimated by the bootstrap method; the errors for the V_P model are the same as those shown in Figure 8a, and the errors for the V_S model were estimated using 100 bootstrap samplings of the data set of Takeo et al. (2018). Takeo et al. (2018) presented models for two different subarrays, but we selected the model for Area-A because it is located at the center of our sampling region. The results for the case using the Area-B model are discussed later. The velocities in the models by Takeo et al. (2018) are the S velocity constrained by the Rayleigh waves under the assumption of the elliptic condition (Thomsen, 1986), which should be assumed to be β_v (i.e., velocity of the horizontally traveling and vertically polarized S wave) instead of V_S. The effects of this approximation are also discussed later.

The synthetic V_P and V_S values in Figures 10a and 10b are computed using several approximations. We assumed the thermal model for the oceanic upper mantle of 130 Ma computed by the plate-cooling model (Parsons & Sclater, 1977) with a plate thickness of 125 km and a potential temperature of 1350°C, which was the preferred model of Takeo et al. (2018) because it explains their model in Area-A. To compute the synthetic V_P and V_S values, we used the elastic parameters presented in Table A1 of Cammarano et al. (2003) and a linear approximation to compute the elastic wave velocities for the given pressure and temperature. We computed the synthetic values for the major upper mantle minerals, that is, olivine (green), garnet (blue), clinopyroxene (purple), and orthopyroxene (light blue). In the computations for olivine, clinopyroxene, and orthopyroxene, we assumed the mole fraction of iron to be 11%. In the computation for garnet, we assumed pure pyrope. In the evaluation, we ignored the anelastic effects and melt. Figures 10a and 10b confirm that the observed P and S velocity contrasts between the lithosphere and asthenosphere are comparable with those of major minerals. However, the vertical gradients of V_P and V_S in the lithospheric region above a depth of approximately 50 km and that of V_P in the asthenospheric region between depths of approximately 90 and 120 km appear to be steeper than the velocity gradient of any major mineral. These anomalous features are demonstrated again in the discussion of V_P/V_S in the next subsection.

5.2. Unique Features in the Observed V_P/V_S Structure

We compared the P model obtained in this study with the S model in Area-A obtained by Takeo et al. (2018) and obtained the V_P/V_S model (Figure 10c). The errors of the obtained V_P/V_S models were estimated using the errors presented in Figures 10a and 10b. We compared our V_P/V_S model (thick red) with the synthetic V_P/V_S values for olivine (green), garnet (blue), clinopyroxene (purple), and orthopyroxene (light blue). Consequently, two unique features were found in the observed V_P/V_S structure.

First, our V_P/V_S model exhibits different features between the lithosphere and asthenosphere. The lithosphere is characterized by a rapid increase in the V_P/V_S values with depth, whereas the asthenosphere is characterized by approximately constant V_P/V_S values. It is especially notable that the vertical gradient observed for the V_P/V_S values in the lithosphere is larger than that of any major mineral. This implies that simple anharmonic effects cannot explain the observation. Because the temperatures in the lithosphere should be significantly below the solidus, anelasticity effects (e.g., Takei, 2017; Yamauchi & Takei, 2016) or melt (e.g., Takei, 2002) are unlikely to be observed; chemical inhomogeneity (i.e., chemical stratification) is required to explain the observation.

Second, our V_P/V_S model exhibits larger values in the vicinity of the LAB. Between depths of approximately 80 and 200 km, the observed V_P/V_S values are larger than the value of any major mineral. This indicates that neither the anharmonic effects nor chemical inhomogeneity can explain the observation. However, because the temperatures in the vicinity of the LAB can be close to or beyond the solidus, the effects of anelasticity or melt can explain the observation. The observed V_P/V_S values between 80 and 200 km are also larger than those of the standard Earth models (isotropic PREM, Dziewonski & Anderson, 1981; IASP91, Kennett & Engdahl, 1991; and AK135, Kennett et al., 1995) (Figure 10d), which again suggest special phenomena in the vicinity of the LAB.

To verify the robustness of the observed features in our V_P/V_S model, we compared our model with the V_P/V_S model obtained using the *S* model in Area-B of Takeo et al. (2018) (Figure 10d). Because Area-A and Area-B were formed at different plate boundaries (Area-A was formed at the Izanagi-Pacific ridge and Area-B was formed at the Pacific-Farallon ridge) (Seton et al., 2012), the comparison tests the bias using different sampling regions of the *P* and *S* models. Both models demonstrated a rapid increase with depth in the lithosphere and larger values in the vicinity of the LAB; thus the robustness of these features was verified. Note that, if we analyzed teleseismic waves, we could develop regional V_P models for Area-A and Area-B, but the obtained V_P models have much poorer vertical resolutions because the vertical resolution of our V_P models are primarily provided by refracted *P* waves with various bottoming depths. We also examined the V_P/V_S models obtained using the V_P models in Figure S10, which were obtained by separately inverting Data Bins 1 and 2 (Figure S14). The differences in V_P/V_S values between the models can be assumed to be an index of the uncertainties due to the lateral heterogeneities. Even though relatively large uncertainties were observed in the shallower part of the lithosphere and the vicinity of the LAB, the general trends appear to be robust.

5.3. Effects of Radial Anisotropy

One of the limitations of our analysis is that a β_v model is used to obtain the V_P/V_S model. It is also an issue that our V_P model is essentially an α_h model because our data set is more sensitive to α_h than α_v. The elliptic condition (Kawakatsu, 2016; Thomsen, 1986) was also arbitrarily assumed (see Figure S1 and Text S1). To estimate the bias resulting from using these assumptions, we corrected our V_P/V_S values using plausible anisotropy parameters to see whether the observed unique features can be still confirmed in the corrected V_P/V_S model.

We used the anisotropy parameters in the model by Nishimura and Forsyth (1989); the ξ, φ, and η values in their oldest oceanic model (>110 Ma) was obtained without assuming parameter correlations (Table 4 of Nishimura & Forsyth, 1989), where ξ, φ, and η are the anisotropy parameters defined in Takeuchi and Saito (1972). Their model exhibits strong *P* radial anisotropy in the lithosphere and strong *S* radial anisotropy in the lithosphere and asthenosphere. The overall features of their model are as follows: β_h is larger than β_v by approximately 2–3% in both the lithosphere and asthenopshere; α_h is larger than α_v by approximately 0–2% in the lithosphere; and η_κ (Kawakatsu, 2016) is approximately 1.00–1.04 in the lithosphere and 1.00 in the asthenosphere.

We assumed our *P* model and the Area-A model of Takeo et al. (2018) to be the α_h and β_v models, respectively, and evaluated the isotropic part of the *P* and *S* velocities using the anisotropic parameters of Nishimura and Forsyth (1989). We then obtained the corrected V_P/V_S model (Figure S15a). Owing to the smaller β_v and larger α_h values in comparison to the isotropic *P* and *S* velocities, the corrected values were systematically smaller than the uncorrected values. However, the systematic shifts were not sufficiently large to alter the primary features; this demonstrates that the radial anisotropy is unlikely to change the conclusions of this study.

5.4. Implications for the Evolution of the Lithosphere-Asthenosphere System

Chemical stratification can be produced in the lithosphere via several processes. Yoshii et al. (1976) proposed the layered structure of the oceanic lithosphere caused by an age-dependent crystallization process. The LABs of the younger oceanic plate are expected to be in the environment at a lower pressure and higher degree of melting. The olivine-rich rocks (e.g., dunite) should be crystallized, while the garnet-rich rocks (e.g., eclogite) are expected at the LABs of the older plate owing to the higher pressure and lower degree

of melting. Therefore, in the older oceanic plate, the rocks crystallized in the shallow lithosphere at younger ages are expected to be more olivine-rich than the underlying garnet-rich rocks that were formed later. This may explain the large lithospheric gradient in V_P/V_S observed in our study region.

5.5. Future Outlook

In this study, only the *P* structures were constrained; further efforts are required to specifically minimize the trade-off with the source side V_S structures. This can be potentially solved by developing an appropriate algorithm to select time windows that are primarily sensitive to the V_P structures. We can also constrain the V_S structures by analyzing *S* and Rayleigh waves. Subsequently, the averaged V_P/V_S values on the raypath can be constrained, which may minimize the bias due to different sampling regions between the V_P and V_S structures. Of course, attempting to constrain 3-D structures using 3-D kernels could be a challenging topic for future research.

Because the *P* velocities in the oceanic upper mantle were not sufficiently constrained in other regions, we cannot ascertain whether the larger V_P/V_S values in the vicinity of the LAB are ubiquitous. Although *P* resolutions are considerably limited, several previous studies (e.g., Gaherty & Jordan, 1996; Nishimura & Forsyth, 1989) have attempted to resolve both *P* and *S* structures, but the obtained V_P/V_S values do not show consistent features (Figure S15b). The systematic deployment of BBOBSs in the Pacific under the Pacific Array initiative (http://eri-ndc.eri.u-tokyo.ac.jp/PacificArray/) is now in progress, and data from such a network will provide important clues for the solution to this problem.

Data Availability Statement

We used the computer systems of the Earthquake Information Center of the Earthquake Research Institute and Information Technology Center, University of Tokyo. All waveform data used in this study are publicly available at OHPDMC (http://ohpdmc.eri.u-tokyo.ac.jp).

Acknowledgments

We thank the associate editor, Dr. J. B. Russl, and two anonymous reviewers for their constructive comments. This research was partially supported by the JSPS KAKENHI Grant Numbers JP15H05832, JP17H02948, JP18H03735, and JP18K03798. We also thank Yasuko Takei and Akiko Takeo for the helpful discussions.

References

Anderson, D. L., & Sammis, C. (1970). Partial melting in the upper mantle. *Physics of the Earth and Planetary Interiors*, *3*, 41–50.

Auer, L., Boschi, L., Becker, T. W., Nissen-Meyer, T., & Giardini, D. (2014). Savani: A variable resolution whole-mantle model of anisotropic shear velocity variations based on multiple data sets. *Journal of Geophysical Research: Solid Earth*, *119*, 3006–3034. https://doi.org/10.1002/2013JB010773

Backus, G. E. (1965). Possible forms of seismic anisotropy of the uppermost mantle under oceans. *Journal of Geophysical Research*, *70*, 3429–3439.

Bijwaard, H., Spakman, W., & Engdahl, E. R. (1998). Closing the gap between regional and global travel time tomography. *Journal of Geophysical Research*, *103*, 30,055–30,078.

Booth, C. M., Forsyth, D. W., & Weeraratne, D. S. (2014). Upper mantle Q structure beneath old seafloor in the western Pacific. *Journal of Geophysical Research: Solid Earth*, *119*, 3448–3461. https://doi.org/10.1002/2013JB010589

Boschi, L., & Dziewonski, A. M. (1999). High- and low-resolution images of the Earth's mantle: Implications of different approaches to tomographic modeling. *Journal of Geophysical Research*, *104*, 25,567–25,594. https://doi.org/10.1029/1999JB900166

Bozdag, E., Peter, D., Lefebvre, M., Komatitsch, D., Tromp, J., Hill, J., et al. (2016). Global adjoint tomography: First-generation model. *Geophysical Journal International*, *207*, 1739–1766.

Cammarano, F., Goes, S., Vacher, P., & Giardini, D. (2003). Inferring uppermantle temperatures from seismic velocities. *Physics of the Earth and Planetary Interiors*, *138*, 197–222.

Chang, S.-J., Ferreira, A. M. G., Ritsema, J., van Heijst, H. J., & Woodhouse, J. H. (2015). Joint inversion for global isotropic and radially anisotropic mantle structure including crustal thickness perturbations. *Journal of Geophysical Research: Solid Earth*, *120*, 4278–4300. https://doi.org/10.1002/2014JB011824

Cline, C. J., Faul, U. H., David, E. C., & Jackson, I. (2018). Redox-influenced seismic properties of upper-mantle olivine. *Nature*, *555*, 355–358.

Dalton, C. A., Ekström, G., & Dziewonski, A. M. (2008). The global attenuation structure of the upper mantle. *Journal of Geophysical Research*, *113*, B09303. https://doi.org/10.1029/2007JB005429

Debayle, E., Dubuffet, F., & Durand, S. (2016). An automatically updated S-wave model of the upper mantle and the depth extent of azimuthal anisotropy. *Geophysical Research Letters*, *43*, 674–682. https://doi.org/10.1002/2015GL067329

Dziewonski, A. M., & Anderson, D. L. (1981). Preliminary reference Earth model. *Physics of the Earth and Planetary Interiors*, *25*, 297–356.

Ekstrom, G., Nettle, M., & Dziewonski, A. M. (2012). The global CMT project 2004–2010: Centroid-moment tensors for 13,017 earthquakes. *Physics of the Earth and Planetary Interiors*, *200-201*, 1–9.

French, S., & Romanowicz, B. (2014). Whole-mantle radially anisotropic shear velocity structure from spectral-element waveform tomography. *Geophysical Journal International*, *199*, 1303–1327.

Fukao, Y., To, A., & Obayashi, M. (2003). Whole mantle P wave tomography using P and PP-P data. *Journal of Geophysical Research*, *108*(B1), 2021. https://doi.org/10.1029/2001JB00098

Gaherty, J. B., & Jordan, T. H. (1996). Seismic structure of the upper mantle in a central Pacific corridor. *Journal of Geophysical Research*, *101*(B10), 22,291–22,309.

Hirth, G., & Kohlstedt, D. L. (1996). Water in the oceanic upper mantle: Implications for rheology, melt extraction and the evolution of the lithosphere. *Earth and Planetary Science Letters*, *144*, 93–108.
Houser, C., Masters, G., Shearer, P., & Laske, G. (2008). Shear and compressional velocity models of the mantle from cluster analysis of long-period waveforms. *Geophysical Journal International*, *174*, 195–212.
Isse, T., Kawakatsu, H., Yoshizawa, T., Takeo, A., Shiobara, H., Sugioka, H., et al. (2019). Surface wave tomography for the Pacific Ocean incorporating seafloor seismic observations and plate thermal evolution. *Earth and Planetary Science Letters*, *510*, 116–130.
Jackson, I., & Faul, U. H. (2010). Grainsize-sensitive viscoelastic relaxation in olivine: Towards a robust laboratory-based model for seismological application. *Physics of the Earth and Planetary Interiors*, *183*, 151–163.
Kawai, K., Takeuchi, N., & Geller, R. J. (2006). Complete synthetic seismograms up to 2 Hz for transversely isotropic spherically symmetric media. *Geophysical Journal International*, *164*, 411–424.
Kawakatsu, H. (2016). A new fifth parameter for transverse isotropy. *Geophysical Journal International*, *204*, 682–685.
Kawakatsu, H., Kumar, P., Takei, Y., Shinohara, M., Kanazawa, T., Araki, E., & Suyehiro, K. (2009). Seismic evidence for sharp lithosphere-asthenosphere boundaries of oceanic plates. *Science*, *324*, 499–502.
Kawakatsu, H., & Utada, H. (2017). Seismic and electrical signatures of the lithosphere-asthenosphere system of the normal oceanic mantle. *Annual Review of Earth and Planetary Sciences*, *45*, 139–167. https://doi.org/10.1146/annurev-earth-063016-020319
Kennett, B. L. N., & Engdahl, E. R. (1991). Traveltimes for global earthquake location and phase identification. *Geophysical Journal International*, *105*(2), 429–465.
Kennett, B. L. N., Engdahl, E. R., & Buland, R. (1995). Constraints on seismic velocities in the Earth from travel-times. *Geophysical Journal International*, *122*(1), 108–124.
Kennett, B. L. N., & Furumura, T. (2013). High-frequency Po/So guided waves in the oceanic lithosphere: I–long-distance propagation. *Geophysical Journal International*, *195*, 1862–1877.
Kennett, B. L. N., Furumura, T., & Zhao, Y. (2014). High-frequency Po/So guided waves in the oceanic lithosphere: II–heterogeneity and attenuation. *Geophysical Journal International*, *199*, 614–630.
Koelemeijer, P., Ritsema, J., Deuss, A., & van Heijst, H.-J. (2016). SP12RTS: A degree-12 model of shear- and compressional-wave velocity for Earth's mantle. *Geophysical Journal International*, *204*, 1024–1039.
Kumar, P., Kawakatsu, H., Shinohara, M., Kanazawa, T., Araki, E., & Suyehiro, K. (2011). P and S receiver function analysis of seafloor borehole broadband seismic data. *Journal of Geophysical Research*, *116*, B12308. https://doi.org/10.1029/2011JB008506
Kustowski, B., Ekström, G., & Dziewonski, A. M. (2008). Anisotropic shear-wave velocity structure of the Earth's mantle: A global model. *Journal of Geophysical Research*, *113*, B06306. https://doi.org/10.1029/2007JB005169
Li, C., van der Hilst, R. D., Engdahl, E. R., & Burdick, S. (2008). A new global model for P wave speed variations in Earth's mantle. *Geochemistry, Geophysics, Geosystems*, *9*, Q05018. https://doi.org/10.1029/2007GC001806
Megnin, C., & Romanowicz, B. (2000). The three-dimensional shear velocity structure of the mantle from the inversion of body, surface and higher-mode waveforms. *Geophysical Journal International*, *143*, 709–728.
Montelli, R., Nolet, G., Dahlen, F. A., & Masters, G. (2006). A catalogue of deep mantle plumes: New results from finite-frequency tomography. *Geochemistry, Geophysics, Geosystems*, *7*, Q11007. https://doi.org/10.1029/2006GC001248
Montelli, R., Nolet, G., Dahlen, F. A., Masters, G., Engdahl, E. R., & Hung, S.-H. (2004). Finite-frequency tomography reveals a variety of plumes in the mantle. *Science*, *303*, 338–343.
Moulik, P., & Ekström, G. (2014). An anisotropic shear velocity model of the Earth's mantle using normal modes, body waves, surface waves and long-period waveforms. *Geophysical Journal International*, *199*, 1713–1738.
Nishimura, C. E., & Forsyth, D. W. (1989). The anisotropic structure of the upper mantle in the Pacific. *Geophysical Journal*, *96*, 203–229.
Obayashi, M., Yoshimitsu, J., Nolet, G., Fukao, Y., Shiobara, H., Sugioka, H., et al. (2013). Finite frequency whole mantle P wave tomography: Improvement of subducted slab images. *Geophysical Research Letters*, *40*, 5652–5657. https://doi.org/10.1002/2013GL057401
Panning, M., & Romanowicz, B. (2004). Base of Earth's mantle based on seismic anisotropy. *Science*, *303*, 351–353.
Parsons, B., & Sclater, J. G. (1977). An analysis of the variation of ocean floor bathymetry and heat flow with age. *Journal of Geophysical Research*, *82*(5), 803–827.
Ritsema, J., Deuss, A., van Heijst, H. J., & Woodhouse, J. H. (2011). Rayleigh wave dispersion, teleseismic traveltime and normal-mode splitting function measurements. *Geophysical Journal International*, *184*, 1223–1236.
Rychert, C. A., & Shearer, P. M. (2009). A global view of the lithosphere-asthenosphere boundary. *Science*, *324*, 495–498.
Schaeffer, A. J., & Lebedev, S. (2013). Global shear speed structure of the upper mantle and transition zone. *Geophysical Journal International*, *194*(2), 417–449.
Seton, M., Muller, R. D., Zahirovic, S., Gaina, C., Torsvik, T., Shephard, G., et al. (2012). Global continental and ocean basin reconstructions since 200 Ma. *Earth-Science Reviews*, *113*, 212–270.
Shimamura, H., Asada, T., Suyehiro, K., Yamada, T., & Inatani, H. (1983). Longshot experiments to study velocity anisotropy in the oceanic lithosphere of the northwestern Pacific. *Physics of the Earth and Planetary Interiors*, *31*, 348–362.
Shinohara, M., Fukano, T., Kanazawa, T., Araki, E., Suyehiro, K., Mochizuki, M., et al. (2008). Upper mantle and crustal seismic structure beneath the Northwestern Pacific Basin using a seafloor borehole broadband seismometer and ocean bottom seismometers. *Physics of the Earth and Planetary Interiors*, *170*, 95–106.
Shintaku, N., Forsyth, D. W., Hajewski, C. J., & Weeraratne, D. S. (2014). Pn anisotropy in Mesozoic western Pacific lithosphere. *Journal of Geophysical Research: Solid Earth*, *119*, 3050–3063. https://doi.org/10.1002/2013JB010534
Shito, A., Suetsugu, D., & Furumura, T. (2015). Evolution of the oceanic lithosphere inferred from Po/So waves traveling in the Philippine Sea Plate. *Journal of Geophysical Research: Solid Earth*, *120*, 5238–5248. https://doi.org/10.1002/2014JB011814
Shito, A., Suetsugu, D., Furumura, T., Sugioka, H., & Ito, A. (2013). Small-scale heterogeneities in the oceanic lithosphere inferred from guided waves. *Geophysical Research Letters*, *40*, 1708–1712. https://doi.org/10.1002/grl.50330
Simmons, N. A., Myers, S. C., Johannesson, G., & Matzel, E. (2012). LLNL-G3Dv3: Global P wave tomography model for improved regional and teleseismic travel time prediction. *Journal of Geophysical Research*, *117*, B10302. https://doi.org/10.1029/2012JB009525
Takei, Y. (2002). Effect of pore geometry on V_P/V_S: From equilibrium geometry to crack. *Journal of Geophysical Research*, *107*(B2), 2043. https://doi.org/10.1029/2001JB000522
Takei, Y. (2017). Effects of partial melting on seismic velocity and attenuation: A new insight from experiments. *Annual Review of Earth and Planetary Sciences*, *45*, 447–470.
Takei, Y., Karasawa, F., & Yamauchi, H. (2014). Temperature, grain size, and chemical controls on polycrystal anelasticity over a broad frequency range extending into the seismic range. *Journal of Geophysical Research: Solid Earth*, *119*, 5414–5443. https://doi.org/10.1002/2014JB011146

Takeo, A., Kawakatsu, H., Isse, T., Nishida, K., Shiobara, H., & Sugioka, H. (2018). In situ characterization of the lithosphere-asthenosphere system beneath NW Pacific Ocean via broadband dispersion survey with two OBS arrays. *Geochemistry, Geophysics, Geosystems*, *19*, 3529–3539. https://doi.org/10.1029/2018GC007588

Takeuchi, N. (2012). Detection of ridge-like structures in the pacific large low-shear-velocity province. *Earth and Planetary Science Letters*, *319*, 55–64.

Takeuchi, N., Geller, R. J., & Cummins, P. R. (1996). Highly accurate P-SV complete synthetic seismograms using modified DSM operators. *Geophysical Research Letters*, *23*, 1175–1178.

Takeuchi, N., Kawakatsu, H., Shiobara, H., Isse, T., Sugioka, H., Ito, A., & Utada, H. (2017). Determination of intrinsic attenuation in the oceanic lithosphere-asthenosphere system. *Science*, *358*(6370), 1593–1596.

Takeuchi, H., & Saito, M. (1972). Seismic surface waves, *Methods in computational physics* (Vol. 11, pp. 217–295). New York: Academic Press.

Tharimena, S., Rychert, C., Harmon, N., & White, P. (2017). Imaging Pacific lithosphere seismic discontinuities—Insights from SS precursor modeling. *Journal of Geophysical Research: Solid Earth*, *122*, 2131–2152. https://doi.org/10.1002/2016JB013526

Thomsen, L. (1986). Weak elastic anisotropy. *Geophysics*, *51*, 1954–1966.

Woodhouse, J. H., & Dziewonski, A. M. (1984). Mapping the upper mantle: Three-dimensional modeling of Earth structure by inversion of seismic waveforms. *Journal of Geophysical Research*, *89*, 5953–5986.

Yamauchi, H., & Takei, Y. (2016). Polycrystal anelasticity at near-solidus temperatures. *Journal of Geophysical Research: Solid Earth*, *121*, 7790–7820. https://doi.org/10.1002/2016JB01331

Yoshii, T., Kono, Y., & Ito, K. (1976). Thickening of the oceanic lithosphere. In H. S. Sutton, et al. (Eds.), *The geophysics of the Pacific Ocean basin and its margin* (pp. 423–430). Washington: American Geophysical Union.